Lawrence Berkeley National Laboratory

Title

Giant Mechano-Optoelectronic Effect in an Atomically Thin Semiconductor

Authors

Wu, Wei

Wang, Jin

Ercius, Peter

et al.

November 13, 2017

Fabio Pulizzi
Chief Editor, Nature Nanotechnology
The Macmillan Building
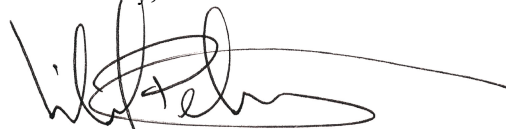4 Crinan Street
London N1 9XW, UK

Dear Dr. Pulizzi,

Enclosed is our manuscript entitled "Giant Mechano-Optoelectronic Effect in an Atomically Thin Semiconductor," which we are submitting for publication in *Nature Nanotechnology*. Our work deals with two main themes which we provide a clear advance in both general scientific understanding and technological capabilities of strain-engineered materials.

1) Experimental techniques involving strain-coupled transport are often criticized since the strain experienced by the material of interest is not known … and is often speculated as being wrong. We provide a new methodology for conducting strain-dependent measurements on thin materials and argue for adoption of a model to standardize experimental studies. This is important as strain is predicted to offer orders of magnitude changes in many important properties across many different scientific fields from catalysis to optics, and lack of confidence in experimental results can mislead or prevent advances in materials design efforts.

2) Observation of a two orders of magnitude increase in the excitonic recombination rate of an indirect semiconductor using mechanical force alone. This is the first time that extrinsic control over an indirect-to-direct electron band gap transition has been conclusively reported, and our theoretical modeling provides general insight for predictive computational materials scientists to design materials with either extremely strain-resistant or extremely strain-sensitive electronic structures not limited to the material we present as a case study in this manuscript.

Given the new paradigm we present, we believe that our manuscript will interest the general readership of *Nature Nanotechnology* and inspire future breakthroughs in the new field of strain-coupled transport in nanomaterials. Thank you for your consideration.

Sincerely,

Michael Thompson Pettes
michael.pettes@uconn.edu

191 AUDITORIUM ROAD, UNIT 3139
UNITED TECHNOLOGIES ENGINEERING BUILDING
STORRS, CT 06269-3139
PHONE 860.486.2090
FAX 860.486.5088
www.engr.uconn.edu/me

An Equal Opportunity Employer

Giant Mechano-Optoelectronic Effect in an Atomically Thin Semiconductor

Authors. Wei Wu[1,2], Jin Wang[2, 3], Peter Ercuis[4], Nicomario C. Wright[1], Danielle M. Leppert-Simenauer[1,5], Robert A. Burke[6,7], Madan Dubey[6], Avinash M. Dogare[2,3], and Michael T. Pettes[1,2*]

Affiliations

[1]Department of Mechanical Engineering, University of Connecticut, Storrs, CT 06269-3139, USA.

[2]Institute of Materials Science, University of Connecticut, Storrs, CT 06269-3136, USA.

[3]Department of Materials Science and Engineering, University of Connecticut, Storrs, CT 06269-3136, USA.

[4]Molecular Foundry, Lawrence Berkeley National Laboratory, Berkeley, CA 94720, USA.

[5]Department of Physics, DePaul University, Chicago, IL 60614, USA.

[6]U.S. Army Research Laboratory, Adelphi, MD 20783, USA.

[7]General Technical Services, LLC, Wall, NJ 07727, USA.

*Correspondence to: michael.pettes@uconn.edu.

Abstract. Transition metal dichalcogenides (TMDs) are particularly sensitive to mechanical strain as they are capable of experiencing high atomic displacements without nucleating defects to release excess energy. Promising for photonic applications, it has been shown that as TMDs are scaled to a thickness of one monolayer, the photoluminescence response is dramatically enhanced due to the emergence of a direct electronic band gap, compared with multi-layer or bulk TMDs which typically exhibit indirect band gaps. Recently, mechanical strain has also been predicted to enable direct excitonic recombination in these materials, where large changes in the photoluminescence response will occur during an indirect-to-direct band gap transition brought on by elastic tensile strain. Here, we demonstrate a two orders of magnitude enhancement in the photoluminescence emission intensity in uniaxially strained single crystalline WSe_2 bilayers.

Through a theoretical model which includes experimentally relevant system conditions, we determine this amplification to arise from a significant increase in direct excitonic recombination. Adding confidence to the high levels of elastic strain achieved in this report, we observe strain-independent mode-dependent Grüneisen parameters over the entire range of tensile strain (1– 3.59 %) which were obtained as 1.149±0.027, 0.307±0.061, and 0.357±0.103 for the E_{2g}, A_{1g}, and A^2_{1g} optical phonon modes, respectively. These results can inform the predictive strain-engineered design of other atomically thin indirect semiconductors, where a decrease in out-of-plane bonding strength will lead to an increase in the strength of strain-coupled optoelectronic effects.

Introduction

Transition metal dichalcogenides (TMDs) are a relatively new class of atomically thin materials receiving interest for overcoming limitations inherent to graphene-based electronics, of which there are more than 40 unique TMDs encompassing a diverse range of unique properties[1-4]. Technologies based on these materials offer size, weight, and power advantages not currently achievable using traditional materials, and are especially promising for nanophotonic applications[5,6] including quantum emission sources[6-16]. As TMDs are scaled to the thickness of one three-atom-thick layer, the electronic dispersion undergoes a transition from an indirect to a direct band gap due to quantum confinement effects[17-20]. In the TMD class, tungsten diselenide (WSe_2) is particularly promising as an optoelectronic material as it can be electrostatically tuned from intrinsic to both high-electron and high-hole concentrations and exhibits an electron-hole effective mass ratio near unity[21,22]. While a direct bandgap can be intrinsically imparted in monolayer materials, it has been predicted that elastic strain[23,24] can be used as an extrinsic method to reversibly engineer a direct band gap in multilayer crystals with indirect band gaps. Promising for optoelectronic applications, atomically thin WSe_2 has recently been shown to exhibit strain-sensitive photoluminescence (PL)[25] and absorbtion[26] responses, and localized strain has been hypothesized to enable spatially precise single photon emission[8,16]. Understanding the mechanisms that are responsible for these effects, however, has been limited by difficulty in quantifying atomic-level strain experienced by an atomically thin material.

Here we report the first experimental observation of a two orders of magnitude direct excitonic recombination enhancement (124.3×) for WSe_2 bilayers at a 3.59% uniaxial tensile strain. This large optoelectronic response enables us to determine the strain-dependent band gap evolution by studying the indirect and direct electron transitions over a wide range of strain. Through a new *ab*

initio model we accurately reproduce the strain-dependent electronic dispersion, which has over predicted strain effects in past reports, and report a strategy to achieve an additional order of magnitude in PL enhancement. Additionally, we have obtained mode-dependent Grüneisen parameters which allow us to validate the strain-dependent properties presented in this report.

Results

In order to demonstrate an indirect-to-direct transition, our study focuses on single crystal bilayer WSe_2 which is an indirect semiconductor in its natural state. The bilayer WSe_2 used here is grown by a chemical vapor deposition (CVD) method similar to previous reports[27,28] (see methods section for details). In contrast to previous multilayer CVD growth reports for TMDs[29], our bilayer WSe_2 are synthesized so that the top and bottom layers possess the same dimensions (up to ~15 μm). Atomic force microscopy (AFM) analysis demonstrates a uniform thickness of ~1.3 nm over the entire triangular crystallite (Figure S1, supporting information). Cross-sectional scanning transmission electron microscopy (STEM) confirms the bilayer structure with an interlayer distance of ~0.7 nm (Figure S2, supporting information). Both AFM and STEM characterizations are in accordance with the out-of-plane unit cell parameter and (0002) interlayer spacing of AB-stacked bulk WSe_2 (1.29825 and 0.64943 nm respectively, Powder Diffraction File no. 38-1388)[30]. Figure 1 illustrates that the spatially dependent Raman spectra of bilayer WSe_2 is uniform in intensity throughout the entire crystallite for the E_{2g}, A_{1g} and A_{1g}^2 Raman active modes.
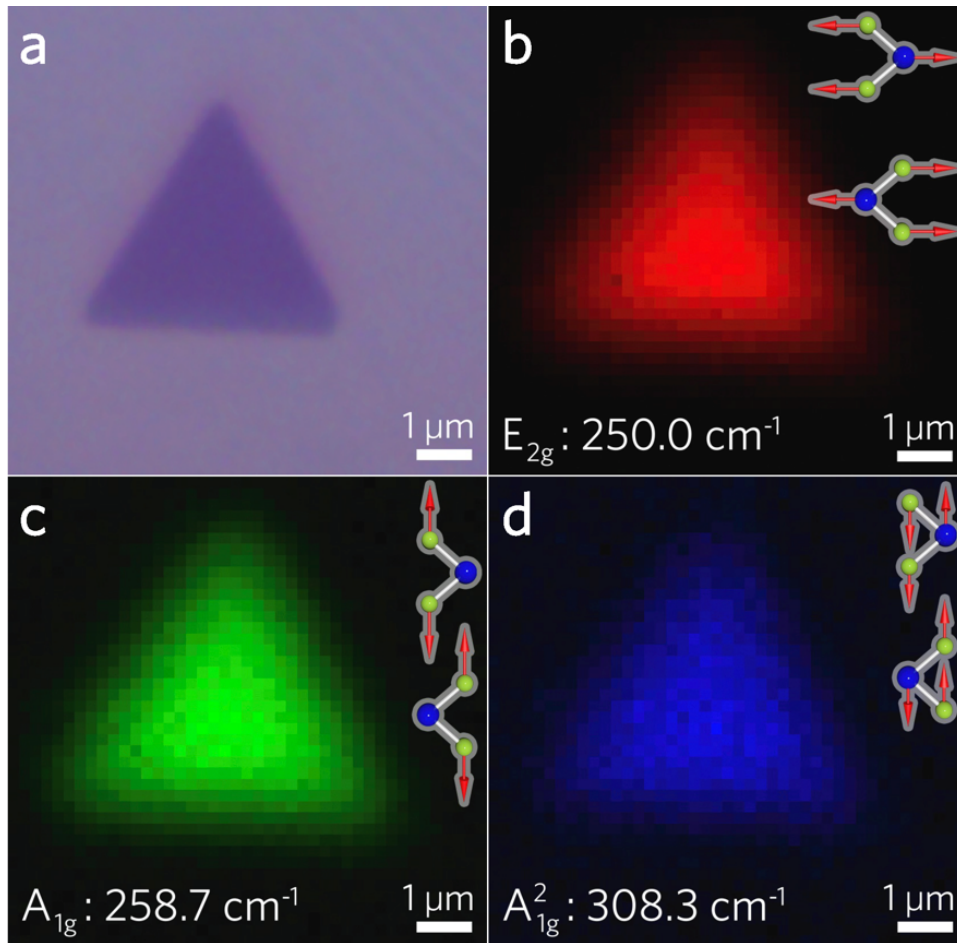
Figure 1. Spatially dependent Raman intensity of bilayer WSe₂. *(a) Optical image of bilayer WSe₂ on a 285 nm SiO₂-on-Si substrate. Spatially resolved Raman intensity at (b) 250 cm⁻¹ (E_{2g} mode), (c) 258.7 cm⁻¹ (A_{1g} mode), and (d) 308.3 cm⁻¹ (A_{1g}^2 mode). Vibrational modes are depicted schematically in panels (b–d).*

Previous studies on strain-coupled properties of atomically thin materials have only been able to access tensile strain up to ~2 %[25,31,32] which limits optoelectronic property amplification or attenuation. One similarity is that these studies consist of an atomically thin material where only one surface is in contact with the substrate or two surfaces are in contact with two different substrate materials. This can lead to a low amount of strain being transferred from the substrate to

the sample as a result of non-ideal interfacial adhesion processing or plastic deformation[33]. This observation erodes confidence in the reported quantitative values unless the amount of transferred strain is validated through vibrational response analysis as has been shown conclusively for graphene[34]. This is more critical for multilayer structures since poor interface adhesion causes a non-uniform strain distribution between the top and bottom layers which can result in slippage between layers[35]. Here, we have developed a method to encapsulate the atomically thin sample with poly(methyl methacrylate) (PMMA) allowing us to apply high strain values without slippage and also prevent surface degradation in our materials, which can occur by exposure to air[36] (see methods section for details).

Uniaxial strain in this study is applied through a custom-designed four-point bending apparatus (Figures S3–S5, supporting information). The strain transferred from the PET substrate to the atomically thin samples was validated by measuring the Grüneisen parameter of graphene using strain-dependent Raman spectra. The graphene was transferred using the same method described for WSe$_2$. The Grüneisen parameter, γ, of the in-plane transverse optical (iTO) phonon polarization was measured as $\gamma_{2D} = 3.894 \pm 0.214$ (Figures S6, supporting information), which is comparable to the value we obtain for graphene by analyzing Ref. 34, $\gamma_{2D} = 3.583 \pm 0.267$, where we have defined the uncertainty from the upper and lower 95% confidence bounds to a linear model. The slight difference between the 2D mode Grüneisen parameter in this work and in Ref. 34 arises from uncertainty in the estimated Poisson ratios for the flexible substrates used[37].

Figure 2 shows the PL emission response to uniaxial tensile strain. The PL spectra were deconvolved by two Gaussian peaks which differ in energy by ~138 meV for the unstrained bilayer WSe$_2$ and by ~8 meV for a strain of 3.59 % (Figure S7, supporting information).
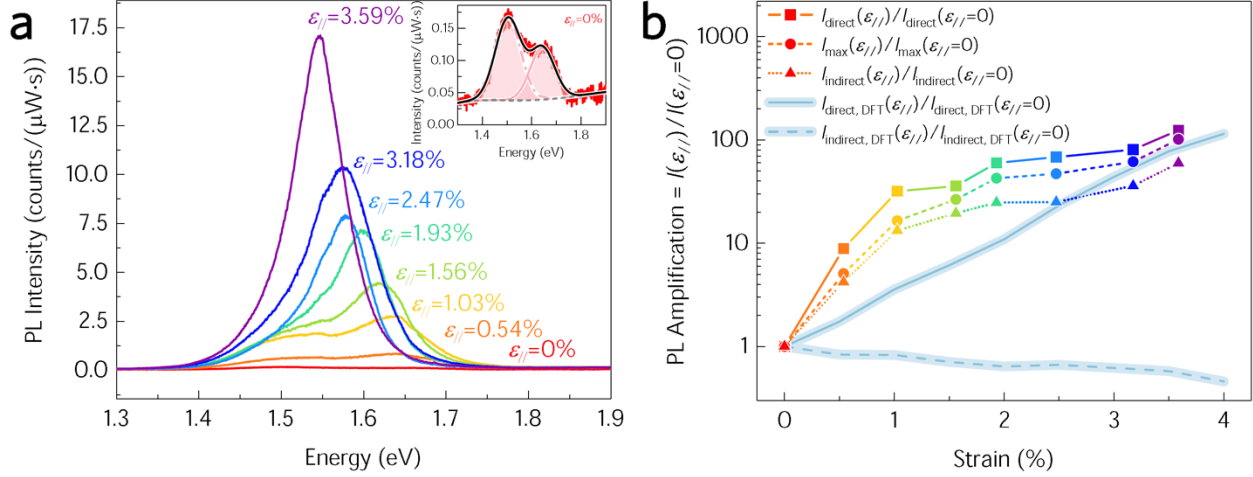
Figure 2. Amplification of the photoluminescence (PL) emission intensity of bilayer WSe₂ when strained up to 3.59%. *(a) PL emission spectra resulting from excitation at 2.33 eV as a function of applied uniaxial strain. Inset shows the PL spectra of the unstrained material, $\varepsilon_{//}=0$, where the indirect (dash-dotted line) and direct (solid line) electronic transitions have been deconvolved using Gaussian distributions. (b) Experimental PL amplification versus strain, defined as $I(\varepsilon_{//})$ / $I(\varepsilon_{//}=0)$. Subscripts max, direct, and indirect denote amplification obtained using the max intensity of the experimental PL, the max intensity of the deconvolved direct sub-peak, and the max intensity of the deconvolved indirect sub-peak, respectively. Computational results obtained by density functional theory (DFT) including the effect of spin orbit coupling, van der Waals interactions, and Poisson effect from PMMA/PET are shown for the direct (solid light blue line) and indirect (dashed light blue line) electronic transitions.*

To elucidate the mechanisms driving the measured strain-coupled optoelectronic effects, we have developed a full theoretical analysis of the electronic dispersion evolution with strain using density functional theory (DFT), the main results of which are shown in Figure 3. Spin orbital coupling (SOC), van der Waals interaction (vdW) of WSe₂ layers, and the Poisson effect of the substrate are all taken into account for the electronic band structure calculation. As Fig. 3b depicts,

the experimental strain-dependent indirect and direct emission peaks match well with the theoretical prediction, with only a slight difference arising from the assumption of strain-independent binding energy and the estimation of the substrate's Poisson ratio. We also compared our experimental results with a previous DFT prediction using the Heyd-Scuseria-Ernzerhof (HSE) hybrid functional which does not consider vdW interactions or the Poisson effect[25] (Figure 3b). The HSE-DFT result predicted an indirect-to-direct transition crossover at a small strain of ~0.5%, which differs from our experimental and theoretical results by an order of magnitude. This large deviation indicates the importance of the vdW interaction for layered TMDs such as bilayer WSe_2 and the Poisson effect of the substrate in achieving physically reproducible theoretical predictions for strain-coupled transport phenomena. We note that it is reasonable to neglect the vdW interaction for un-encapsulated monolayer TMDs, however, this component is critical for multilayer TMDs.
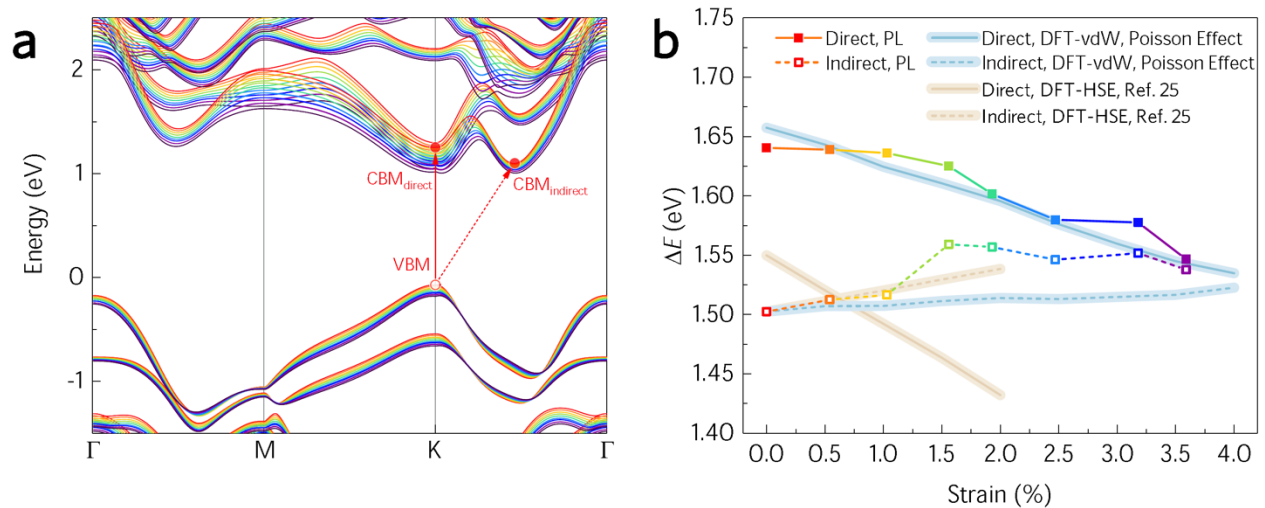
Figure 3. Indirect-to-direct electronic band transition conversion through strain. *(a) Evolution of the electronic band structure in response to uniaxial strain calculated using density functional theory including both spin orbit coupling, interlayer van der Waals interactions, and the Poisson*

effect (DFT-vdW-Poisson) for $\varepsilon_{//}$ = 0% (red) to 4% (purple) in increments of 0.5%. Direct and indirect electronic transitions are depicted. (b) Strain-dependence of the interband transition energies normalized to that of the unstrained indirect PL transition. Experimental values have been obtained by deconvolution of the PL emission spectra using Gaussian distributions and are shown in comparison with a DFT-vdW-Poisson model and a calculation neglecting van der Waals interactions (DFT-HSE[25]). The indirect-to-direct conversion occurs at $\varepsilon_{//}$ > 3.5% in both the experiment and DFT-vdW-Poisson calculation and at ~0.5% when vdW interactions are neglected (DFT-HSE[25]), indicating that increased interlayer coupling strength may lead to weaker strain-coupled effects in layered materials.

To assign the two PL sub peaks to electronic transitions, we first compared the PL peak energy difference to the spin-orbit valence band splitting energy at the K-point in the Brillouin zone, which is ~0.5 eV from 0 to 2% uniaxial tensile strain[26]. The valance band splitting energy is at least four times larger than our measured PL peak energy difference, and its dependence on strain is much less than we measured here. Secondly, neither of the two PL peaks are expected to result from trion emission since the charged exciton energy is only ~30 meV lower than the exciton energy for unstrained bilayer WSe_2[38], which is ~4.6 times lower than we have measured. Thirdly, these two PL peaks do not belong to biexcitonic recombination since its observability should significantly diminish above 70 K[39]. We can also conclude that these two peaks do not stem from slippage between the top and bottom WSe_2 layers at high strain. As slippage will increase with strain, the difference between these two peaks would revert to a larger energy closer to that of the unstrained material, which is contradictory with our experimental observation of continuously decreasing separation with strain. As shown in the inset of Figure 2a, the unstrained PL peak at 1.50 eV has a full width at half maximum (FWHM) of 121.03 meV, which is similar to the reported

FWHM of the indirect band transition of unstrained bilayer WSe$_2$[40]. Additionally, the strain-dependent blue (red) shift of the lower (higher) energy PL sub peak also matches the indirect (direct) electronic band gap strain dependence calculated by our *ab initio* model which includes spin-orbit coupling, interlayer van der Waals bonding, and the Poisson effect from the PMMA encapsulation layer (Figure 3). Thus, we assign the lower energy PL sub peak to the indirect electron transition between the conduction band minimum at the Σ-point (CBM$_\Sigma$) and the valence band maximum at the K-point (VBM$_K$), and the higher energy sub peak to the direct electronic transition at the K-point (CBM$_K$–VBM$_K$). The PL indirect band gap linearly increased with strain at a rate of 11.14 meV/% to 1.54 eV (FWHM = 123.08 meV) at 3.59% uniaxial tensile strain. The PL direct band gap decreased with strain at a rate of 27.9 meV/% from 1.64 eV (FWHM = 117.2 meV) in the unstrained material to 1.54 eV (FWHM = 53.6 meV) at 3.59 % uniaxial tensile strain. The FWHM of the direct transition peak is similar to that reported for mechanically exfoliated monolayer WSe$_2$ (FWHM = 56 meV)[40]. Our theoretical model predicts that the PL indirect-to-direct crossover will occur at 4.28 %, however, the ability to reach this value experimentally is limited by the fatigue of the PMMA/PET substrate.

Since the bilayer WSe$_2$ is by definition an indirect semiconductor under uniaxial strain up to 3.59%, we report optical strain-coupled behavior for direct and indirect transitions separately. Figure 2b shows the PL intensity corresponding to the direct excitonic transition (colored squares) is enhanced by 124.3 times at 3.59% strain. The enhancement of the overall maximum PL intensity (colored triangles) is 101.4 times at 3.59% strain. Even at 1.93% uniaxial strain, the maximum PL intensity enhancement is ~42.6 times, which is 42% larger than previously reported at 2% strain[25] due to the high amount of strain transferred to the TMD sample in this work as verified experimentally using thin graphite (see methods section and supporting information for details).

The maximum PL intensity enhancement is smaller than the enhancement of the direct transition since the indirect transition has a higher PL intensity than the direct transition for the unstrained sample. As the strain increases to values higher than ~0.5%, the direct transition begins to dominate the PL response as shown in Figure 2a.

To elucidate the mechanisms responsible for the large enhancement observed here and to understand the maximum achievable amplification, we have used our DFT-vdW-Poisson theoretical model to calculate the enhancements of the direct and indirect excitonic transitions as

$$\frac{I_j(\varepsilon_{//})}{I_j(\varepsilon_{//}=0)} = \frac{e^{-\frac{\Delta E_j(\varepsilon_{//})}{k_{\mathrm{B}}T}}}{e^{-\frac{\Delta E_j(\varepsilon_{//}=0)}{k_{\mathrm{B}}T}}}, \quad j = \text{direct, indirect} \tag{1}$$

where $\Delta E_j(\varepsilon_{//})$ and $\Delta E_j(\varepsilon_{//}=0)$ are the band transition energies of the strained and unstrained bilayer WSe$_2$ (see supporting information for details). The PL intensity enhancement for the experimental direct transition (colored squares in Figure 2b) and theoretical prediction results (light blue solid line in Figure 2b) are consistent. The experimental PL enhancement is 124.3 times and the calculated result is 81.35 times at 3.59% strain. The deviation at lower strain may arise from simplifying assumptions for Equation 1 and the assumption of a strain-independent binding energy in the DFT-vdW-Poisson model.

As can be seen in Figure 2b for the indirect transition, a large disagreement in both trend and magnitude between the experimental (colored triangles) and calculated (light blue solid line) amplification of the indirect transition likely arises due to enhanced scattering between K and Σ valleys in the conduction band, which become closer in energy with strain as will be discussed. This mechanism is also likely responsible for reducing the overall experimentally observed PL amplification in comparison with calculated amplification of the direct transition for strains above 2%. The experimental PL intensity of the indirect transition is amplified by ~59.7 times at 3.59%

11

strain, which is contrary to both our experimental observation and theoretical prediction of an increase in indirect band gap energy with tensile strain. Applying Equation 1 to the indirect transition, the PL intensity is expected to attenuate with tensile strain to a value of $I_{\text{indirect}}/I_{\text{indirect}}(\varepsilon_{//}=0) = 0.52$ at 3.59% strain. This can be explained by an increase in the phonon-assisted electron scattering from the conduction band minimum at the K-point (CBM$_{\text{direct}}$) to the conduction band minimum at the Σ-point (CBM$_{\text{indirect}}$) as illustrated in Figure 3a. The PL intensity of the indirect transition is the result of competition between: (i) an increase in the indirect band gap with strain which weakens the radiative recombination rate and (ii) phonon-assisted CBM$_{\text{direct}}$-to-CBM$_{\text{indirect}}$ electron scattering which enhances the indirect recombination rate. The phonon-assisted CBM$_{\text{direct}}$-to-CBM$_{\text{indirect}}$ intervalley transition rate is proportional to the direct transition rate which increases with strain. Thus, the indirect transition PL intensity is enhanced with strain. Meanwhile, increasing the indirect band gap with strain counteracts the PL intensity enhancement due to the phonon-assisted CBM$_{\text{direct}}$-to-CBM$_{\text{indirect}}$ intervalley transitions. The energy difference between CBM$_{\text{direct}}$ and CBM$_{\text{indirect}}$ drives this intraband electron transition and can be evaluated as

$$\Delta E_{\text{CBM}_{\text{direct}}-\text{CBM}_{\text{indirect}}} = \Delta E_{\text{direct}-\text{indirect}} = E_{\text{direct}} - E_{\text{indirect}} . \tag{2}$$

Our theoretical results shown in Figure 3b indicate that $\Delta E_{\text{indirect-direct}}$ decreases with increased strain at a rate of 35.7 meV/%, from 155 meV at $\varepsilon_{//}=0\%$ to 12.2 meV at $\varepsilon_{//}=4\%$. Thus, the phonon-assisted CBM$_{\text{direct}}$-to-CBM$_{\text{indirect}}$ transition rate is expected to increase with tensile strain by 250.6 times at 4% uniaxial tensile strain according to

$$\frac{I_{\text{intraband}}(\varepsilon_{//})}{I_{\text{intraband}}(\varepsilon_{//}=0)} = \frac{e^{-\frac{\Delta E_{\text{CBM}_{\text{direct}}-\text{CMB}_{\text{indirect}}}(\varepsilon_{//})}{k_{\text{B}}T}}}{e^{-\frac{\Delta E_{\text{CBM}_{\text{direct}}-\text{CMB}_{\text{indirect}}}(\varepsilon_{//}=0)}{k_{\text{B}}T}}} . \tag{3}$$

The consequences of increased intraband scattering can be observed in Figure 2b, where the maximum PL enhancement becomes closer to the direct transition enhancement at high strain while entering into an apparent saturation regime as the valley minima near degeneracy. Additionally, the high amplification of the indirect transition intensity with strain (as opposed to the theoretically predicted attenuation) results from the greatly increased intraband scattering processes as $\Delta E_{\text{indirect-direct}}$ decreases towards degeneracy.
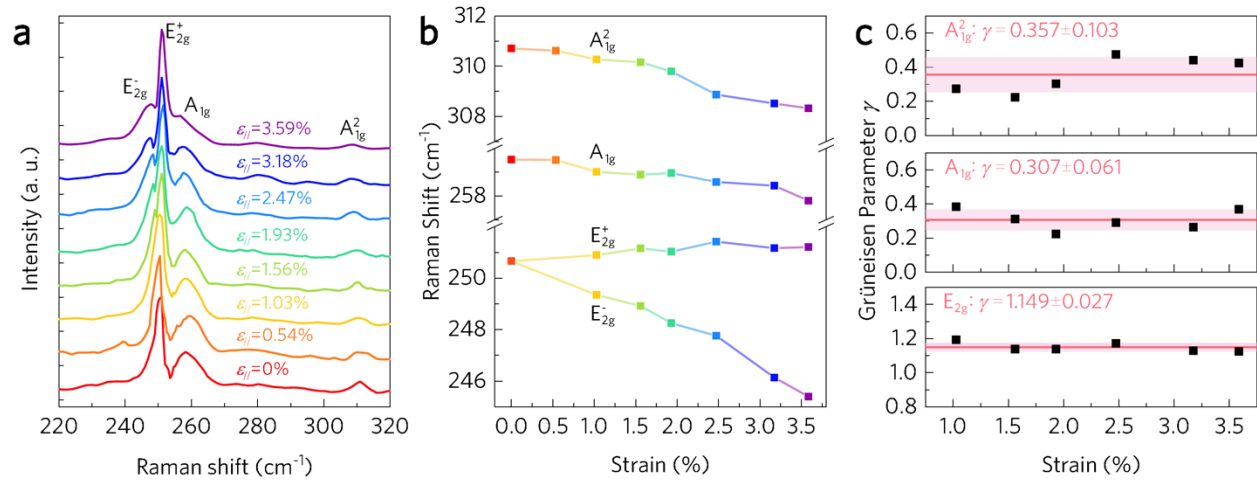
Figure 4. Raman spectra of bilayer WSe$_2$ as it is strained up to 3.59%. *(a) Raman spectra as a function of uniaxial strain ($\varepsilon_{//}$). As strain increases, the in-plane E_{2g} optical phonon mode evolves into separate E_{2g}^{+} and E_{2g}^{-} modes. (b) Strain dependence of the peak Raman shifts for the E_{2g}^{+}, E_{2g}^{-}, A_{1g}, and A_{1g}^{2} modes, obtained by deconvolution of the experimental Raman spectra using Lorentzian distributions. The linear strain dependence of the Raman shift indicates strain relaxation by slippage or plastic deformation is not observed. (c) Mode-specific Grüneisen parameters of bilayer WSe$_2$ are constant over the range of $0.01 \leq \varepsilon_{//} \leq 0.036$.*

Strain-dependence of the phonon energies in bilayer WSe$_2$ yield information on atomic displacement and fundamental thermodynamic properties. Figure 4 shows the evolution of optical

phonon energies with strain as obtained by Raman spectroscopy. The unstrained sample shows three major Raman active modes: (i) the in-plane transverse optical E_{2g} mode at 250.1 cm^{-1}, (ii) the out-of-plane transverse A_{1g} mode at 259.5 cm^{-1}, and (iii) the out-of-plane transverse A_{1g}^2 mode at 310.7 cm^{-1}. The E_{2g} and A_{1g} peak energies are comparable to those reported for unstrained CVD-grown[27] and mechanically exfoliated WSe$_2$ thin layers[40], while the A_{1g}^2 mode only appears for multilayer WSe$_2$[27,41]. As increasing the uniaxial tensile strain breaks the crystal symmetry, the doubly degenerate E_{2g} mode evolves into two discrete modes, E_{2g}^+ and E_{2g}^-, corresponding to the in-plane atomic vibrations perpendicular and parallel to the applied strain direction, respectively. Both the E_{2g}^+ and E_{2g}^- modes exhibit a consistent shift with strain (Figure 4b), indicating a lack of Raman-observable slippage between the WSe$_2$/PMMA, PMMA/PET, and WSe$_2$/WSe$_2$ interfaces over a large range of strain (0%-3.59%). The redshift of the E_{2g}^- mode arises from phonon softening in the presence of tensile strain ($\varepsilon_{//}$), while the blueshift of the E_{2g}^+ mode indicates stiffening due to perpendicular compressive strain ($\varepsilon_{\perp\perp}$) resulting from the Poisson effect of the substrate. In contrast with previous un-encapsulated cases that only consider the in-plane two-dimensional Poisson effect[34], we have evaluated the Grüneisen parameter of our encapsulated bilayer WSe$_2$ with a three-dimensional Poisson effect model developed to incorporate the compressive strain in the out-of-plane direction arising from the strained encapsulation layer. Using this three-dimensional Poisson effect model, the phonon polarization specific Grüneisen parameters are evaluated as

$$
\gamma_i = \begin{cases} -\dfrac{\Delta\omega_{0,i}^+ + \Delta\omega_{0,i}^-}{2\varepsilon_{//}(1 - \nu_{\text{in-plane}} - \nu_{\text{out-of-plane}})\omega_{0,i}}, & i = E_{2g} \\[4ex] -\dfrac{\Delta\omega_{0,i}}{\varepsilon_{//}(1 - \nu_{\text{in-plane}} - \nu_{\text{out-of-plane}})\omega_{0,i}}, & i = A_{1g}, A_{1g}^2 \end{cases}, \tag{4}
$$

14

where $\omega_{0,i}$ is the frequency of the unstrained phonon mode i, $\Delta\omega_{0,i}$ is the change in frequency of the phonon mode i with uniaxial strain, $v_{\text{in-plane}}$ is the Poisson's ratio of the PMMA/PET composite, and $v_{\text{out-of-plane}}$ is the Poisson's ratio of the PMMA (see supporting information for details). Over the range of 0–3.59% strain, the Grüneisen parameter (γ) of the E_{2g} mode is measured as 1.149 with a standard deviation of 0.027, γ of the A_{1g} mode is 0.307 with a standard deviation of 0.061, and γ of the A_{1g}^{2} mode is 0.357 with a standard deviation of 0.103, which are comparable with MoS_2[31]. We justify the importance of our 3D model for encapsulated atomically thin materials as follows. If we applied a two-dimensional Poisson effect model to our experimental data, the Grüneisen parameter of our samples would be calculated as 0.517±0.012, 0.138±0.027 and 0.161±0.046 for the E_{2g}, A_{1g} and A^{2}_{1g} modes respectively. Thus, by neglecting the out-of-plane Poisson effect in encapsulated samples, the Grüneisen parameter would be underestimated by a factor of 2.2.

Conclusions

In conclusion, we have demonstrated that a two orders of magnitude photoluminescence enhancement in bilayer WSe_2 stems from strain-dependent electronic band gap evolution in the elastic regime. The encapsulation technique and four-point bending method developed for this study enable us to apply up to ~3.59% uniaxial strain on our atomically thin material while preventing sample degradation from exposure to air during thermal processing and laser irradiation. We have postulated an important materials design guideline related to band degeneracy as suppression of intervalley electron scattering events through band engineering will lead to further increases in emission enhancement. Our study also demonstrates the necessity of

considering van der Waals interactions and the Poisson effect in the atomically thin material's surrounding environment for theoretical predictions of strain-coupled optoelectronic phenomena.

Methods

CVD growth of bilayer tungsten diselenide (WSe$_2$). WSe$_2$ bilayers are grown by a chemical vapor deposition (CVD) method which can also be described as powder vaporization. A crucible containing 200 mg of WO$_3$ powder (Sigma Aldrich, 99.9% purity) is placed in the center of a one-zone furnace fitted with a 1-inch diameter quartz tube. Another crucible containing 200 mg of Se powder (Alfa Aesar, 99.999% purity) is placed upstream at the edge of heating zone, which operates at a lower temperature during growth. Crystal growth occurs on a silicon substrate with a ~285 nm-thick SiO$_2$ film placed polished-side-down on the crucible containing the WO$_3$ powder. Prior to growth, the CVD reactor is pumped to a rough vacuum pressure lower than 10^{-4} mbar, followed by injection of gaseous H$_2$ (4.992%)/N$_2$ (balance) (Airgas, 99.999% purity) at 100 cm^{3}min^{-1} to purge the system. Once atmospheric pressure is reached, the H$_2$/N$_2$ flow is reduced to 50 cm^{3}min^{-1}, and the growth is performed using a sealed bubbler filled with silicone oil (Sigma Aldrich) at the exhaust to maintain 1 atm pressure and prevent air from diffusing back into the reaction chamber. The system is heated to 1000°C in 1 hour, then keep at 1000°C for 15 minutes. During the growth, the Se temperature is measured as ~290°C by a thermocouple taped to the outside of the quartz tube. The system is cooled to 750°C in 20 minutes; followed by rapid cooling achieved by opening the furnace lid. We have identified that a critical parameter in successful growth of bilayer WSe$_2$ single crystals with uniform thickness is the time at which Se vapor is introduced into the chamber, which can be finely tuned by adjusting the position of the Se crucible. We achieve high yield growth by introducing Se when the furnace center's thermocouple reads ~820°C. We observe that introducing Se too early in the growth results in small grain sizes and

non-uniform thickness likely due to poisoning of the metal oxide source powder, which reduces the tungsten precursor concentration. Introducing Se too late results in thicker samples as thick tungsten oxyselenide nucleation on the substrate is reduced to WSe_2.

Photoluminescence and Raman characterization. The PL emission and Raman spectra of WSe_2 bilayer are obtained using a multiline Raman spectrometer (LabRAM HR Evolution, Horiba Scientific, Ltd.) with a 2.33 eV ($\lambda = 532$ nm) continuous wave excitation at low power (86 µW) to avoid sample damage and spectral shifts due to local heating effects[31].

Encapsulation of WSe_2 bilayers. CVD-grown WSe_2 bilayers were transferred between two thin PMMA layers and attached to a thick flexible poly(ethylene terephthalate) (PET) substrate (see supporting information for additional details). High strain in the samples was achieved after annealing the composite at 150°C under an argon atmosphere to enhance the adhesion strength between the interfaces of PET, PMMA, and WSe_2 without sample degradation by exposure to air at high temperature. We observed the PMMA layer became conformal to the substrate and passed standard Scotch[TM] and Kapton® tape peeling tests after annealing, indicating strong adhesion, as has been observed for PMMA-assisted transfer of graphene[42].

Strain transfer verification. To verify the strain transferred to an atomically thin material in our experimental configuration, we first obtained the Grüneisen parameter of graphene using the measured strain-dependent Raman spectra. The Grüneisen parameter, γ, of the in-plane transverse optical (iTO) phonon polarization was determined using the 2D mode of the sample and our three-dimensional Poisson effect model as $\gamma_{2D} = 3.894 \pm 0.214$ (Figures S6, supporting information). This is comparable to the value we obtain for graphene by analyzing Ref. 34, $\gamma_{2D} = 3.583 \pm 0.267$, where we have defined the uncertainty from the upper and lower 95% confidence bounds. We note that Ref. 34 has demonstrated near ideal strain transfer to graphene by comparing the experimental γ

of the G mode ($\gamma_{E2g} = 1.99$) with that calculated by *ab initio* modeling ($\gamma_{E2g,DFT} = 1.87$) which adds further justification to our validation approach. However, as the G mode signal was blocked by the background signals from the PMMA/PET substrate in our experiment, we were not able to directly measure the Grüneisen parameter of the G mode.

References

1. Geim, A. K. & Grigorieva, I. V. Van der Waals heterostructures. *Nature* **499**, 419–425 (2013). http://dx.doi.org/10.1038/nature12385

2. Chhowalla, M., Shin, H. S., Eda, G., Li, L.-J., Loh, K. P., & Zhang, H. The chemistry of two-dimensional layered transition metal dichalcogenide nanosheets. *Nature Chemistry* **5**, 263–275 (2013). http://dx.doi.org/10.1038/nchem.1589

3. Butler, S. Z., Hollen, S. M., Cao, L., Cui, Y., Gupta, J. A., Gutiérrez, H. R., Heinz, T. F., Hong, S. S., Huang, J., Ismach, A. F., Johnston-Halperin, E., Kuno, M., Plashnitsa, V. V., Robinson, R. D., Ruoff, R. S., Salahuddin, S., Shan, J., Shi, L., Spencer, M. G., Terrones, M., Windl, W., & Goldberger, J. E. Progress, challenges, and opportunities in two-dimensional materials beyond graphene. *ACS Nano* **7**, 2898–2926 (2013). http://dx.doi.org/10.1021/nn400280c

4. Bhimanapati, G. R., Lin, Z., Meunier, V., Jung, Y., Cha, J., Das, S., Xiao, D., Son, Y., Strano, M. S., Cooper, V. R., Liang, L., Louie, S. G., Ringe, E., Zhou, W., Kim, S. S., Naik, R. R., Sumpter, B. G., Terrones, H., Xia, F., Wang, Y., Zhu, J., Akinwande, D., Alem, N., Schuller, J. A., Schaak, R. E., Terrones, M., & Robinson, J. A. Recent advances in two-dimensional materials beyond graphene. *ACS Nano* **9**, 11509–11539 (2015). http://dx.doi.org/10.1021/acsnano.5b05556

5. Lee, C.-H., Lee, G.-H., van der Zande, A. M., Chen, W., Li, Y., Han, M., Cui, X., Arefe, G., Nuckolls, C., Heinz, T. F., Guo, J., Hone, J., & Kim, P. Atomically thin p–n junctions with van der Waals heterointerfaces. *Nature Nanotechnology* **9**, 676–681 (2014). http://dx.doi.org/10.1038/nnano.2014.150

6. Palacios-Berraquero, C., Barbone, M., Kara, D. M., Chen, X., Goykhman, I., Yoon, D., Ott, A. K., Beitner, J., Watanabe, K., Taniguchi, T., Ferrari, A. C., & Atatüre, M. Atomically thin quantum light-emitting diodes. *Nature Communications* **7**, 12978-1–6 (2016). http://dx.doi.org/10.1038/ncomms12978

7. Branny, A., Kumar, S., Proux, R., & Gerardot, B. D. Deterministic strain-induced arrays of quantum emitters in a two-dimensional semiconductor. *Nature Communications* **8**, 15053-1−7 (2017). http://dx.doi.org/10.1038/ncomms15053

8. Palacios-Berraquero, C., Kara, D. M., Montblanch, A. R. P., Barbone, M., Latawiec, P., Yoon, D., Ott, A. K., Loncar, M., Ferrari, A. C., & Atatüre, M. Large-scale quantum-emitter arrays in atomically thin semiconductors. *Nature Communications* **8**, 15093-1–6 (2017). http://dx.doi.org/10.1038/ncomms15093

9. Tonndorf, P., Schmidt, R., Schneider, R., Kern, J., Buscema, M., Steele, G. A., Castellanos-Gomez, A., van der Zant, H. S. J., Michaelis de Vasconcellos, S., & Bratschitsch, R. Single-photon emission from localized excitons in an atomically thin semiconductor. *Optica* **2**, 347–352 (2015). http://dx.doi.org/10.1364/OPTICA.2.000347

10. Srivastava, A., Sidler, M., Allain, A. V., Lembke, D. S., Kis, A., & Imamoğlu, A. Optically active quantum dots in monolayer WSe_2. *Nature Nanotechnology* **10**, 491–496 (2015). http://dx.doi.org/10.1038/nnano.2015.60

11. Koperski, M., Nogajewski, K., Arora, A., Cherkez, V., Mallet, P., Veuillen, J. Y., Marcus, J., Kossacki, P., & Potemski, M. Single photon emitters in exfoliated WSe_2 structures. *Nature Nanotechnology* **10**, 503–506 (2015). http://dx.doi.org/10.1038/nnano.2015.67

12. Chakraborty, C., Kinnischtzke, L., Goodfellow, K. M., Beams, R., & Vamivakas, A. N. Voltage-controlled quantum light from an atomically thin semiconductor. *Nature Nanotechnology* **10**, 507–511 (2015). http://dx.doi.org/10.1038/nnano.2015.79

13. He, Y.-M., Clark, G., Schaibley, J., R., He, Y., Chen, M.-C., Wei, Y.-J., Ding, X., Zhang, Q., Yao, W., Xu, X., Lu, C.-Y., & Pan, J.-W. Single quantum emitters in monolayer semiconductors. *Nature Nanotechnology* **10**, 497–502 (2015). http://dx.doi.org/10.1038/nnano.2015.75

14. Tran, T. T., Bray, K., Ford, M. J., Toth, M., & Aharonovich, I. Quantum emission from hexagonal boron nitride monolayers. *Nature Nanotechnology* **11**, 37–41 (2016). http://dx.doi.org/10.1038/nnano.2015.242

15. Tonndorf, P., Schwarz, S., Kern, J., Niehues, I., del Pozo-Zamudio, O., Dmitriev, A. I., Bakhtinov, A. P., Borisenko, D. N., Kolesnikov, N. N., Tartakovskii, A. I., de Vasconcellos, S. M., & Bratschitsch, R. Single-photon emitters in GaSe. *2D Materials* **4**, 021010-1–6 (2017). http://dx.doi.org/10.1088/2053-1583/aa525b

16. Kumar, S., Kaczmarczyk, A., & Gerardot, B. D. Strain-induced spatial and spectral isolation of quantum emitters in mono- and bilayer WSe_2. *Nano Letters* **15**, 7567–7573 (2015). http://dx.doi.org/10.1021/acs.nanolett.5b03312

17. Mak, K. F., Lee, C., Hone, J., Shan, J., & Heinz, T. F. Atomically thin MoS_2: A new direct-gap semiconductor. *Physical Review Letters* **105**, 136805-1–4 (2010). http://dx.doi.org/10.1103/PhysRevLett.105.136805

18. Gutierrez, H. R., Perea-Lopez, N., Elias, A. L., Berkdemir, A., Wang, B., Lv, R., Lopez-Urias, F., Crespi, V. H., Terrones, H., & Terrones, M. Extraordinary room-temperature

photoluminescence in triangular WS_2 monolayers. *Nano Letters* **13**, 3447–3454 (2013). http://dx.doi.org/10.1021/nl3026357

19. Zhao, W., Ghorannevis, Z., Chu, L., Toh, M., Kloc, C., Tan, P.-H., & Eda, G. Evolution of electronic structure in atomically thin sheets of WS_2 and WSe_2. *ACS Nano* **7**, 791–797 (2013). http://dx.doi.org/10.1021/nn305275h

20. Tongay, S., Sahin, H., Ko, C., Luce, A., Fan, W., Liu, K., Zhou, J., Huang, Y.-S., Ho, C.-H., Yan, J., Ogletree, D. F., Aloni, S., Ji, J., Li, S., Li, J., Peeters, F. M., & Wu, J. Monolayer behaviour in bulk ReS_2 due to electronic and vibrational decoupling. *Nature Communications* **5**, 3252-1–6 (2014). http://dx.doi.org/10.1038/ncomms4252

21. Fang, H., Tosun, M., Seol, G., Chang, T. C., Takei, K., Guo, J., & Javey, A. Degenerate n-doping of few-layer transition metal dichalcogenides by potassium. *Nano Letters* **13**, 1991–1995 (2013). http://dx.doi.org/10.1021/nl400044m

22. Yu, L., Zubair, A., Santos, E. J. G., Zhang, X., Lin, Y., Zhang, Y., & Palacios, T. High-performance WSe_2 complementary metal oxide semiconductor technology and integrated circuits. *Nano Letters* **15**, 4928–4934 (2015). http://dx.doi.org/10.1021/acs.nanolett.5b00668

23. Johari, P. & Shenoy, V. B. Tuning the electronic properties of semiconducting transition metal dichalcogenides by applying mechanical strains. *ACS Nano* **6**, 5449–5456 (2012). http://dx.doi.org/10.1021/nn301320r

24. Dong, L., Dongare, A. M., Namburu, R. R., Regan, T. P., & Dubey, M. Theoretical study on strain induced variations in electronic properties of $2H\text{-}MoS_2$ bilayer sheets. *Applied Physics Letters* **104**, 053107-1–5 (2014). http://dx.doi.org/10.1063/1.4863827

25. Desai, S. B., Seol, G., Kang, J. S., Fang, H., Battaglia, C., Kapadia, R., Ager, J. W., Guo, J., & Javey, A. Strain-induced indirect to direct bandgap transition in multilayer WSe$_2$. *Nano Letters* **14**, 4592–4597 (2014). http://dx.doi.org/10.1021/nl501638a

26. Schmidt, R., Niehues, I., Schneider, R., Drüppel, M., Deilmann, T., Rohlfing, M., de Vasconcellos, S. M., Castellanos-Gomez, A., & Bratschitsch, R. Reversible uniaxial strain tuning in atomically thin WSe$_2$. *2D Materials* **3**, 021011-1–7 (2016). http://dx.doi.org/10.1088/2053-1583/3/2/021011

27. Liu, B., Fathi, M., Chen, L., Abbas, A., Ma, Y., & Zhou, C. Chemical vapor deposition growth of monolayer WSe$_2$ with tunable device characteristics and growth mechanism study. *ACS Nano* **9**, 6119–6127 (2015). http://dx.doi.org/10.1021/acsnano.5b01301

28. Chen, J., Liu, B., Liu, Y., Tang, W., Nai, C. T., Li, L., Zheng, J., Gao, L., Zheng, Y., Shin, H. S., Jeong, H. Y., & Loh, K. P. Chemical vapor deposition of large-sized hexagonal WSe$_2$ crystals on dielectric substrates. *Advanced Materials* **27**, 6722–6727 (2015). http://dx.doi.org/10.1002/adma.201503446

29. Bilgin, I., Liu, F., Vargas, A., Winchester, A., Man, M. K., Upmanyu, M., Dani, K. M., Gupta, G., Talapatra, S., Mohite, A. D., & Kar, S. Chemical vapor deposition synthesized atomically thin molybdenum disulfide with optoelectronic-grade crystalline quality. *ACS Nano* **9**, 8822–8832 (2015). http://dx.doi.org/10.1021/acsnano.5b02019

30. Wong-Ng, W., McMurdie, H. F., Paretzkin, B., Zhang, Y., Davis, K. L., Hubbard, C. R., Dragoo, A. L., & Stewart, J. M. Reference X-ray diffraction powder patterns of fifteen ceramic phases. *Powder Diffraction* **2**, 257–265 (1987). http://dx.doi.org/10.1017/S0885715600012926

31. Conley, H. J., Wang, B., Ziegler, J. I., Haglund, R. F., Jr., Pantelides, S. T., & Bolotin, K. I. Bandgap engineering of strained monolayer and bilayer MoS_2. *Nano Letters* **13**, 3626–3630 (2013). http://dx.doi.org/10.1021/nl4014748

32. Li, Y., Hu, Z., Lin, S., Lai, S. K., Ji, W., & Lau, S. P. Giant anisotropic Raman response of encapsulated ultrathin black phosphorus by uniaxial strain. *Advanced Functional Materials* **27**, 1616–3028 (2016). http://dx.doi.org/10.1002/adfm.201600986

33. Huang, M., Yan, H., Chen, C., Song, D., Heinz, T. F., & Hone, J. Phonon softening and crystallographic orientation of strained graphene studied by Raman spectroscopy. *Proceedings of the National Academy of Sciences* **106**, 7304–7308 (2009). http://dx.doi.org/10.1073/pnas.0811754106

34. Mohiuddin, T. M. G., Lombardo, A., Nair, R. R., Bonetti, A., Savini, G., Jalil, R., Bonini, N., Basko, D. M., Galiotis, C., Marzari, N., Novoselov, K. S., Geim, A. K., & Ferrari, A. C. Uniaxial strain in graphene by Raman spectroscopy: *G* peak splitting, Grüneisen parameters, and sample orientation. *Physical Review B* **79**, 205433-1–8 (2009). http://dx.doi.org/10.1103/PhysRevB.79.205433

35. McCreary, A., Ghosh, R., Amani, M., Wang, J., Duerloo, K.-A. N., Sharma, A., Jarvis, K., Reed, E. J., Dongare, A. M., & Banerjee, S. K. Effects of uniaxial and biaxial strain on few-layered terrace structures of MoS_2 grown by vapor transport. *ACS Nano* **10**, 3186–3197 (2016). http://dx.doi.org/10.1021/acsnano.5b04550

36. Kang, K., Godin, K., Kim, Y. D., Fu, S., Cha, W., Hone, J., & Yang, E.-H. Graphene-assisted antioxidation of tungsten disulfide monolayers: Substrate and electric-field effect. *Advanced Materials* **29**, 1603898-1–8 (2017). http://dx.doi.org/10.1002/adma.201603898

37. Mounet, N. & Marzari, N. First-principles determination of the structural, vibrational and thermodynamic properties of diamond, graphite, and derivatives. *Physical Review B* **71**, 205214-1–14 (2005). http://dx.doi.org/10.1103/PhysRevB.71.205214

38. Jones, A. M., Yu, H., Ross, J. S., Klement, P., Ghimire, N. J., Yan, J., Mandrus, D. G., Yao, W., & Xu, X. Spin–layer locking effects in optical orientation of exciton spin in bilayer WSe_2. *Nature Physics* **10**, 130–134 (2014). http://dx.doi.org/10.1038/nphys2848

39. You, Y., Zhang, X.-X., Berkelbach, T. C., Hybertsen, M. S., Reichman, D. R., & Heinz, T. F. Observation of biexcitons in monolayer WSe_2. *Nature Physics* **11**, 477–481 (2015). http://dx.doi.org/10.1038/nphys3324

40. Pospischil, A., Furchi, M. M., & Mueller, T. Solar-energy conversion and light emission in an atomic monolayer p-n diode. *Nature Nanotechnology* **9**, 257–261 (2014). http://dx.doi.org/10.1038/nnano.2014.14

41. Terrones, H., Del Corro, E., Feng, S., Poumirol, J. M., Rhodes, D., Smirnov, D., Pradhan, N. R., Lin, Z., Nguyen, M. A., Elias, A. L., Mallouk, T. E., Balicas, L., Pimenta, M. A., & Terrones, M. New first order Raman-active modes in few layered transition metal dichalcogenides. *Scientific Reports* **4**, 4215-1–9 (2014). http://dx.doi.org/10.1038/srep04215

42. Suk, J. W., Kitt, A., Magnuson, C. W., Hao, Y., Ahmed, S., An, J., Swan, A. K., Goldberg, B. B., & Ruoff, R. S. Transfer of CVD-grown monolayer graphene onto arbitrary substrates. *ACS Nano* **5**, 6916–6924 (2011). http://dx.doi.org/10.1021/nn201207c

Supplementary Information for:

Giant Mechano-Optoelectronic Effect in an Atomically Thin Semiconductor

Authors. Wei Wu[1,2], Jin Wang[2,3], Peter Ercius[4], Nicomario C. Wright[1], Danielle M. Leppert-Simenauer[1,5], Robert A. Burke[6], Madan Dubey[6,7], Avinash M. Dogare[2,3], and Michael T. Pettes[1,2*]

Affiliations

[1]Department of Mechanical Engineering, University of Connecticut, Storrs, CT 06269-3139, USA.

[2]Institute of Materials Science, University of Connecticut, Storrs, CT 06269-3136, USA.

[3]Department of Materials Science and Engineering, University of Connecticut, Storrs, CT 06269-3136, USA.

[4]Molecular Foundry, Lawrence Berkeley National Laboratory, Berkeley, CA 94720, USA.

[5]Department of Physics, DePaul University, Chicago, IL 60614, USA.

[6]U.S. Army Research Laboratory, Adelphi, MD 20783, USA.

[7]General Technical Services, LLC, Wall, NJ 07727, USA.

*Correspondence to: michael.pettes@uconn.edu.

I. Atomic force microscopy characterization of WSe$_2$ bilayer

The thickness of WSe$_2$ atomic-thin was measured by using Asylum Cypher^{TM} atomic force microscopy at AC air tapping mode. Figure S1 shows a WSe$_2$ bilayer crystallite with a uniform thickness of ~1.3 nm, in accordance with the out-of-plane unit cell parameter of AB-stacked bulk WSe$_2$, 12.9825 Å (Powder Diffraction File no. 38-1388)[1].
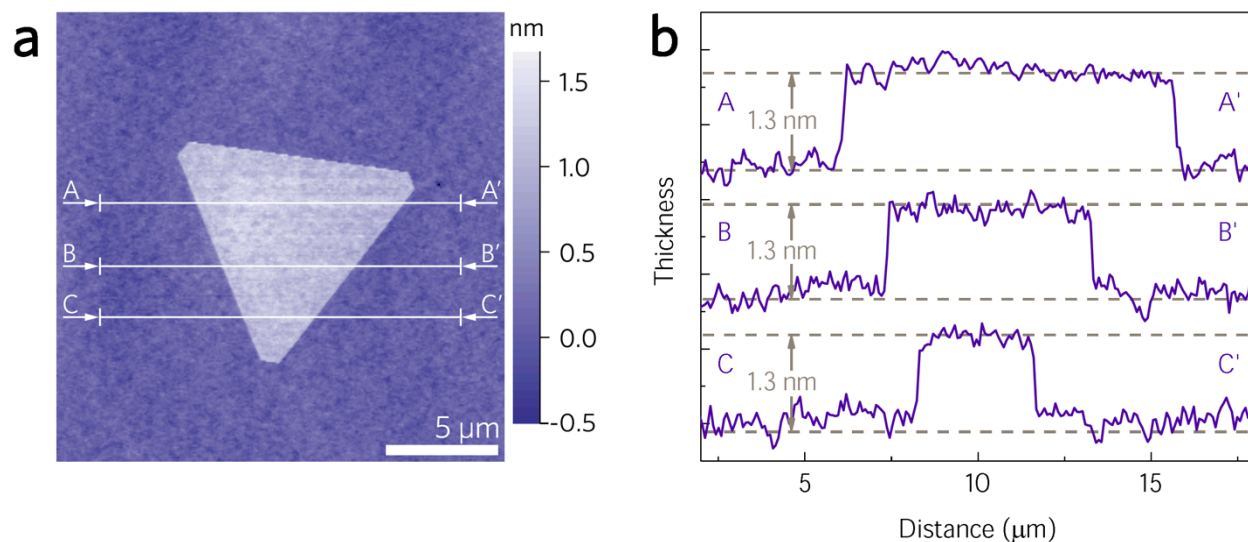
Figure S1. Atomic force microscopy (AFM) analysis of uniform bilayer WSe₂. *(A) AFM mapping of the entire domain demonstrates uniform thickness across the crystallite. (B) Cross-sectional height profiles demonstrate the thickness of bilayer WSe$_2$ is approximately 1.3 nm and is consistent with the c-axis unit cell parameter for AB-stacked WSe$_2$ (1.2983 nm, Powder Diffraction File #38-1388)[1].*

II. Cross-sectional scanning transmission electron microscopy (STEM) characterization

The cross-sectional STEM sample is prepared using a Ga$^+$ Focused Ion Beam (FIB, FEI Helios Nanolab 460F1). The WSe$_2$ on SiO$_2$/Si crystal is first aligned so that the lamella can be prepared along a certain crystallographic direction, namely $\langle 10\overline{1}0 \rangle$ or $\langle 2\overline{1}\overline{1}0 \rangle$. To prevent sample damage caused by gallium ion bombardment, the WSe$_2$ is first coated with carbonaceous platinum by electron beam induced metal deposition (EBIMD) at 5 kV and 13 nA. As shown in Figure S2a, the triangular shape of the WSe$_2$ bilayer is still observable after EBIMD of platinum. A thicker Pt coating, ~2 μm in thickness, is subsequently deposited using the Ga$^+$ ion beam at 30 kV and 80 pA and acts as the sacrificial protective layer for ion milling. The lamella is then cut by the Ga$^+$ beam at 30 kV and 2.5 nA. The lamella is lifted off and loaded onto the side of a FIB lift-out TEM

grid as a 'flag' to avoid copper re-deposition from the grid during the thinning and polishing processes. During the polishing step, the Ga^+ ion beam milling power is gradually reduced to 8 kV and 21 pA to avoid sample damage. STEM images were acquired using the Molecular Foundry's Transmission Electron Aberration-corrected Microscope (TEAM) 0.5 at 80 kV. STEM analysis clearly reveals the bilayer structure with an interlayer distance ~0.7 nm (Figure S2b,c).
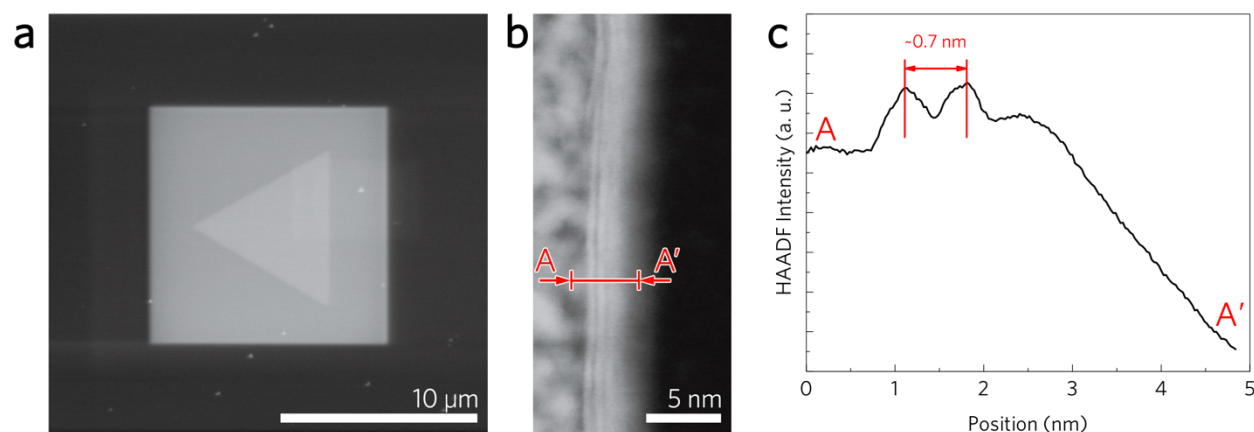
Figure S2. Cross-sectional scanning transmission microscopy (STEM) of a WSe₂ bilayer. *(a) Scanning electron micrograph showing a single crystal WSe₂ bilayer (bright triangle) and a thin electron-beam deposited platinum coating (bright square) used in the cross-sectioning process. (b) Cross-sectional high-angular annular dark-filed (HAADF) STEM analysis shows the bilayer structure of the CVD-grown WSe₂. (c) Line profile of the HAADF intensity along the length of the red line drawn in (b). The interlayer distance is measured as ~0.7 nm and is in agreement with the {0002} interplanar spacing of WSe₂ (d_{0002}=0.6493 nm, Powder Diffraction File #38-1388)[1].*

III. Sample transfer and encapsulation method
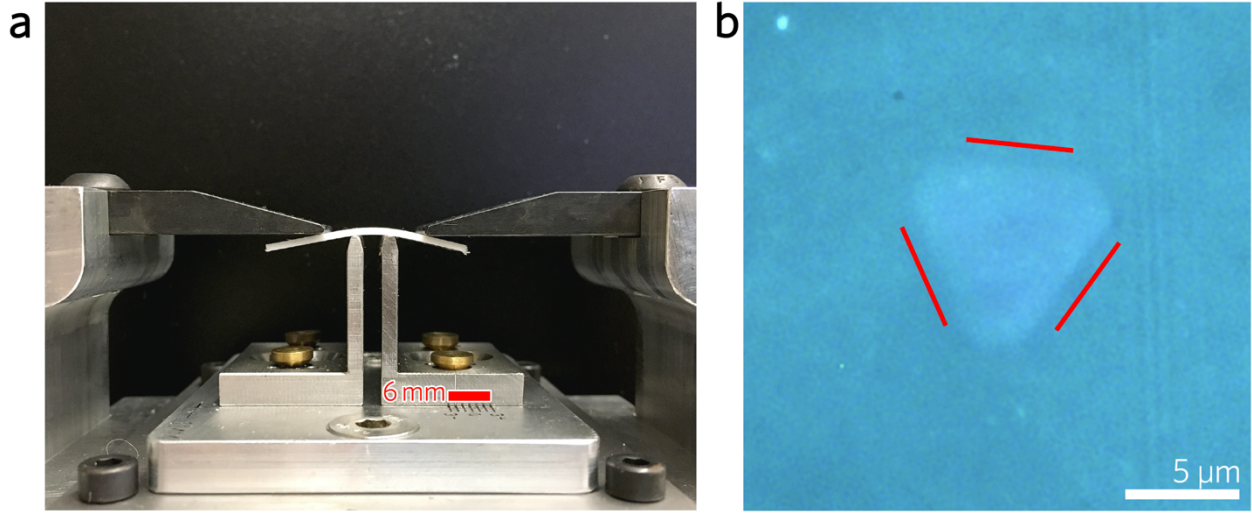
A thin layer of poly(methyl methacrylate) (PMMA, ~500 nm) is spin-coated onto the WSe₂/SiO₂/Si sample at 500 rpm with a slow ramping rate of 15 rpm/s to prevent sample delamination or interlayer exfoliation and does not undergo a pre-exposure baking step. The coated

substrate is then immersed into 1% HF to etch the SiO_2, followed by thoroughly rinsing the PMMA/WSe$_2$ composite in deionized H_2O. Meanwhile, another thin PMMA layer (~500 nm) is spin-coated onto a 1.00±0.01 mm-thick poly(ethylene terephthalate) (PET, Sigma Aldrich #GF74053818) substrate which serves as the bottom flexible substrate used to apply strain in this experiment. The PMMA/WSe$_2$ composite is then transferred onto PMMA/PET substrate and naturally dried under an argon atmosphere to prevent WSe$_2$ degradation. To obtain high strain transfer from the substrate to the encapsulated sample, the PMMA/WSe$_2$/PMMA/PET composite is annealed at 150°C for several hours until both the top and bottom PMMA layers become conformal[2]. The encapsulated WSe$_2$ bilayer is still observable by an optical microscope after the annealing process as shown in Figure S3. We have found that lowering the PMMA annealing temperature below 150°C results in poor strain transfer from the substrate to the WSe$_2$, while increasing to temperatures higher than 150°C induces irreversible deformation of the PMMA/WSe$_2$/PMMA/PET composite. After the annealing treatment, the PMMA encapsulation layer is strongly attached to the PET substrate and passes standard Scotch^{TM} and Kapton$^{®}$ tape peeling tests.

IV. Four-point bending system

A custom-designed four-point bending apparatus was used to apply tensile strain to bilayer WSe$_2$. The bending apparatus consists of two horizontal upper arms to apply the downward force, and two vertical lower supports whose height is adjusted using a precision vertical linear stage (Newport #M-MVN80) with 10 μm vertical graduations. Figure S3 shows the system with a strained PMMA/WSe$_2$/PMMA/PET composite. The bend radius is determined using image processing software (ImageJ 1.51k)[3], and the uniaxial strain on the WSe$_2$ is determined as $\varepsilon_{//} = \tau/(2r)$ where τ is the composite thickness, measured to be ~1 mm. We note that this value of strain

is limited to the case of perfect strain transfer from the substrate to the encapsulated WSe$_2$. We have performed a calibration study using graphene which demonstrates our experiment is conducted in this regime (see section VI in the supporting information).

Figure S3. Custom four-point bending apparatus. *(a) Photograph of the experimental apparatus applying uniaxial strain to a poly(methyl methacrylate) (PMMA)-encapsulated bilayer WSe$_2$ sample affixed to a flexible poly(ethylene terephthalate) (PET) substrate. Tick marks machined into the right of the device (below scale bar) indicate mm. (b) Optical microscope image of a bilayer WSe$_2$ crystallite encapsulated by two thin PMMA layers on a flexible PET substrate. The crystal is outlined in red as a guide to the eye.*

V. Three-dimensional Poisson effect model for Grüneisen parameter calculation

The Grüneisen parameter (γ) describes the effect of changes in cell volume on the phonon energies. The macroscopic Grüneisen parameter is defined as[4]

$$\gamma = V\left(\frac{\partial P}{\partial E}\right)_V = \frac{V}{C_V}\left(\frac{\partial S}{\partial V}\right)_T, \tag{S1}$$

where P is the pressure, E is the internal energy, V is the volume of crystal, C_V is the specific heat at constant volume, S is the entropy, and T is the temperature. From the quasi-harmonic approximation, the entropy, S, can be expressed as[5]

$$S = -k_B \sum_i \sum_k \left\{ \ln\left[1 - \exp\left(-\frac{\hbar\omega_{k,i}}{k_B T} \right) \right] + \frac{\hbar\omega_{k,i}}{k_B T} \exp\left(\frac{\hbar\omega_{k,i}}{k_B T} \right) \left[\exp\left(\frac{\hbar\omega_{k,i}}{k_B T} \right) - 1 \right]^{-1} \right\},$$

(S2)

and its volume derivative at constant temperature can be expressed as

$$\left(\frac{dS}{dV} \right)_T = -k_B \sum_i \sum_k \frac{1}{\omega_{k,i}} \frac{\partial\omega_{k,i}}{\partial V} \frac{\left(\frac{\hbar\omega_{k,i}}{k_B T} \right)^2 \exp\left(\frac{\hbar\omega_{k,i}}{k_B T} \right)}{\left[\exp\left(\frac{\hbar\omega_{k,i}}{k_B T} \right) - 1 \right]^2},$$

(S3)

where k_B is the Boltzmann constant, $\hbar$ is the reduced Planck constant, i denotes the phonon mode index, k denotes the phonon wave vector, and $\omega_{k,i}$ is the angular frequency of phonon mode i at wavevector k. The macroscopic Grüneisen parameter, γ, can be further expanded according to equations S1–S3 as

$$\gamma = \frac{V}{C_V} \left(\frac{\partial S}{\partial V} \right)_T = -\frac{k_B}{C_V} \sum_i \sum_k \frac{V}{\omega_{k,i}} \frac{\partial\omega_{k,i}}{\partial V} \frac{\left(\frac{\hbar\omega_{k,i}}{k_B T} \right)^2 \exp\left(\frac{\hbar\omega_{k,i}}{k_B T} \right)}{\left[\exp\left(\frac{\hbar\omega_{k,i}}{k_B T} \right) - 1 \right]^2}.$$

(S4)

Based on Einstein's model[6], where all oscillators have the same energy, $\omega_{k,i} = \omega_{0,i}$ and the vibrational density of states is defined as $g(\omega_{0,i}) = \delta(\omega - \omega_{0,i})$. The specific heat can be expressed as

$$C_V = \left(\frac{\partial U}{\partial T} \right)_V = \left(\frac{\partial}{\partial T} \sum_i \sum_k \hbar\omega_{k,i} g(\omega_{k,i}) \left[\exp\left(\frac{\hbar\omega_{k,i}}{k_B T} \right) - 1 \right]^{-1} \right)_V$$

$$= k_B \sum_i \left(\frac{\hbar\omega_{0,i}}{\kappa_B T} \right)^2 \frac{\exp\left(\frac{\hbar\omega_{0,i}}{k_B T} \right)}{\left[\exp\left(\frac{\hbar\omega_{0,i}}{k_B T} \right) - 1 \right]^2}.$$

(S5)

Thus, in the Einstein limit of a non-propagating optical phonon with frequency $\omega_{0,i}$, the microscopic Grüneisen parameter can be expressed as

$$\gamma_i = -\frac{V}{\omega_{0,i}}\frac{\partial \omega_{0,i}}{\partial V} = -\frac{\Delta \omega_{0,i}}{\varepsilon_h \omega_{0,i}}, \tag{S6}$$

where ε_h is the hydrostatic component of strain and $\Delta \omega_{0,i}$ is the phonon frequency change due to strain. In our study, the phonon polarizations of interest are the in-plane transverse optical E_{2g} mode and the out-of-plane transverse optical A_{1g} and A_{1g}^2 modes.
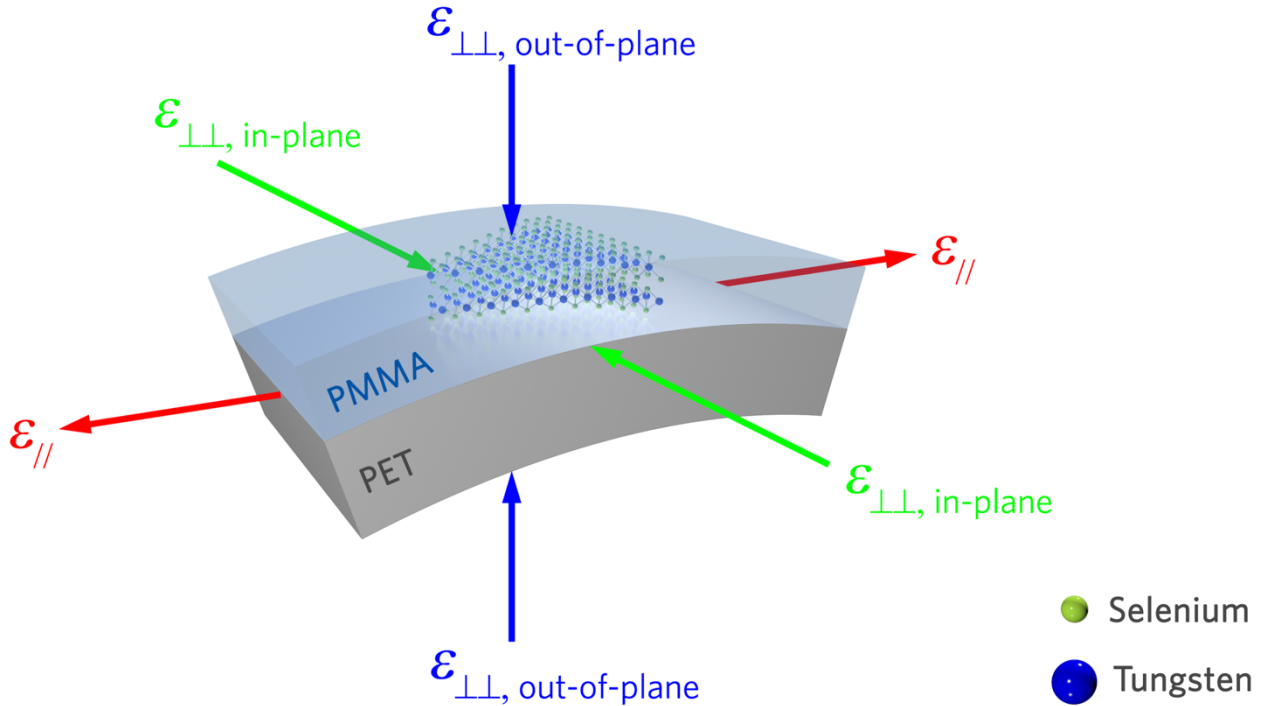
Figure S4. Schematic of the Poisson effect on a uniaxially strained WSe_2 bilayer encapsulated in PMMA on top of a PET substrate: *$\varepsilon_{//}$ is the uniaxial strain applied through the four-point bending apparatus, $\varepsilon_{\perp\perp,\ in\text{-}plane}$ is the in-plane compressive strain caused by the Poisson effect of the PMMA/PET composite, and $\varepsilon_{\perp\perp,\ out\text{-}of\text{-}plane}$ is the out-of-plane compressive strain from the Poisson effect on the PMMA encapsulation layer.*

For a non-encapsulated and tensile-strained sample, an in-plane perpendicular compressive strain component ($\varepsilon_{\perp\perp,\text{ in-plane}}$) arises due to the Poisson effect of the substrate, which should be considered when estimating the Grüneisen parameter of strained atomically thin materials placed onto flexible substrates. It has been shown that the in-plane compressive strain component in the substrate can overcome the counter force from covalent bonds within monolayer graphene[7] and MoS_2[8]. For an encapsulated and tensile-strained sample, an additional out-of-plane compressive strain ($\varepsilon_{\perp\perp,\text{ out-of-plane}}$) will arise due to the Poisson effect of the encapsulation layer as illustrated in Figure S4. The counterforce for this out-of-plane strain is the interlayer van der Waals bonds, which are orders of magnitude weaker in energy than the covalent bonds. Thus, for encapsulated layered materials, it is necessary to consider both the in-plane and the out-of-plane Poisson effects. In this study, ε_{h} has three components depicted in Figure S4: (i) $\varepsilon_{//}$, the uniaxial tensile strain applied by the bending substrate, (ii) $\varepsilon_{\perp\perp,\text{in-plane}}$, the compressive strain due to the Poisson effect of the PMMA/PET substrate in the sample plane and perpendicular to $\varepsilon_{//}$, and (iii) $\varepsilon_{\perp\perp,\text{out-of-plane}}$, the compressive strain due to the Poisson effect of the PMMA encapsulation layer perpendicular to both the sample plane and $\varepsilon_{//}$. The hydrostatic strain and Grüneisen parameter can then be expressed as

$$\varepsilon_{\text{h}} = \varepsilon_{//} + \varepsilon_{\perp\perp,\text{in-plane}} + \varepsilon_{\perp\perp,\text{out-of-plane}} = \varepsilon_{//}\left(1 - \nu_{\text{in-plane}} - \nu_{\text{out-of-plane}}\right) \text{ and} \tag{S7}$$

$$\gamma_i = -\frac{\Delta\omega_{0,i}}{\varepsilon_{//}(1 - \nu_{\text{in-plane}} - \nu_{\text{out-of-plane}})\omega_{0,i}}, \tag{S8}$$

respectively, where $\nu_{\text{in-plane}}$ is the Poisson's ratio within the sample plane, and $\nu_{\text{out-of-plane}}$ is the Poisson's ratio along the direction perpendicular to sample plane. The semi-crystalline PET used here has a Poisson's ratio between 0.37–0.44 (range provided by manufacturer, Goodfellow Cambridge Ltd.). As the PET substrate is ~10^3 times thicker than the PMMA layers, we have

chosen $\nu_{\text{in-plane}} = 0.4$ for the PMMA/PET composite. Since the WSe$_2$ crystals are well-separated and cover only a small region of the PMMA layer, we treat the PMMA/WSe$_2$/PMMA composite as a PMMA block instead of a heterogeneous structure. Thus, the Poisson's ratio for the out-of-plane compressive strain, $\nu_{\text{out-of-plane}}$, was chosen as 0.33 since this value is commonly used for spin-coated PMMA[9]. The measured Raman spectra enables us to calculate the exact phonon frequency change with applied mechanical stimulus for Raman active modes. The E$_{2g}$ Raman active mode is an in-plane vibration. Since the E$_{2g}$ mode decomposes into separate E$_{2g}^{+}$ and E$_{2g}^{-}$ peaks under uniaxial strain, we can define the frequency shifts and Grüneisen parameter of the E$_{2g}$ mode as[7]

$$
\Delta\omega_{0,\text{E}_{2g}}^{\pm} = \Delta\omega_{0,\text{E}_{2g}}^{\text{h}} \pm \frac{1}{2}\Delta\omega_{0,\text{E}_{2g}}^{\text{s}} \qquad\qquad \text{and} \qquad (S9)
$$

$$
= -\omega_{0,\text{E}_{2g}}\gamma_{\text{E}_{2g}}\left(\varepsilon_{//} + \varepsilon_{\perp\perp,\text{in-plane}} + \varepsilon_{\perp\perp,\text{out-of-plane}}\right) \pm \frac{1}{2}\frac{\partial\omega_{0,\text{E}_{2g}}^{\text{s}}}{\partial\varepsilon_{\text{s}}}\left(\varepsilon_{//} - \varepsilon_{\perp\perp,\text{in-plane}} - \varepsilon_{\perp\perp,\text{out-of-plane}}\right)
$$

respectively, where $\Delta\omega_{0,\text{E}_{2g}}^{\text{h}}$ and $\Delta\omega_{0,\text{E}_{2g}}^{\text{s}}$ are the phonon frequency changes corresponding to the hydrostatic component and shear component of strain, respectively. The phonon frequency of the E$_{2g}$ mode at 0% strain is denoted as $\omega_{0,\text{E}_{2g}}$. The Grüneisen parameters of the in-plane E$_{2g}$ optical phonon mode and the out-of-plane A$_{1g}$ and A$_{1g}^{2}$ optical phonon modes can be now be expressed as

$$
\gamma_i = -\frac{\Delta\omega_{0,i}^{+} + \Delta\omega_{0,i}^{-}}{2\varepsilon_{//}(1 - \nu_{\text{in-plane}} - \nu_{\text{out-of-plane}})\omega_{0,i}}, \quad i = \text{E}_{2g} \text{ and} \qquad (S10)
$$

$$
\gamma_i = -\frac{\Delta\omega_{0,i}}{\varepsilon_{//}(1 - \nu_{\text{in-plane}} - \nu_{\text{out-of-plane}})\omega_{0,i}}, \quad i = \text{A}_{1g}, \text{A}_{1g}^{2}. \qquad (S11)
$$

The above equations also apply to the non-encapsulated samples, where one can simply set the Poisson's ratio of the encapsulation layer, $\nu_{\text{out-of-plane}}$, to zero which reduces equations S10 and S11 to previously reported expressions[7,8].

VI. Strain reversibility and strain transfer verification

The strain reversibility verification was carried out through PL emission spectra measurements under repeated strains. The PL emission spectra and the maximum PL intensity in Figure S5 show that the strain effect is reversible until 1.56% strain. The PL spectra does not exhibit hysteresis in cyclic straining, indicating no slippage between two WSe$_2$ layers or between the WSe$_2$ bilayer and the PMMA. After 1.56% strain, the PET or PMMA enters the plastic regime so cyclic testing is not performed at strain values of 1.93% or above, but we do not observe creep or relaxation as evidenced by our Raman spectra at high strains (see Figure 4, main text).
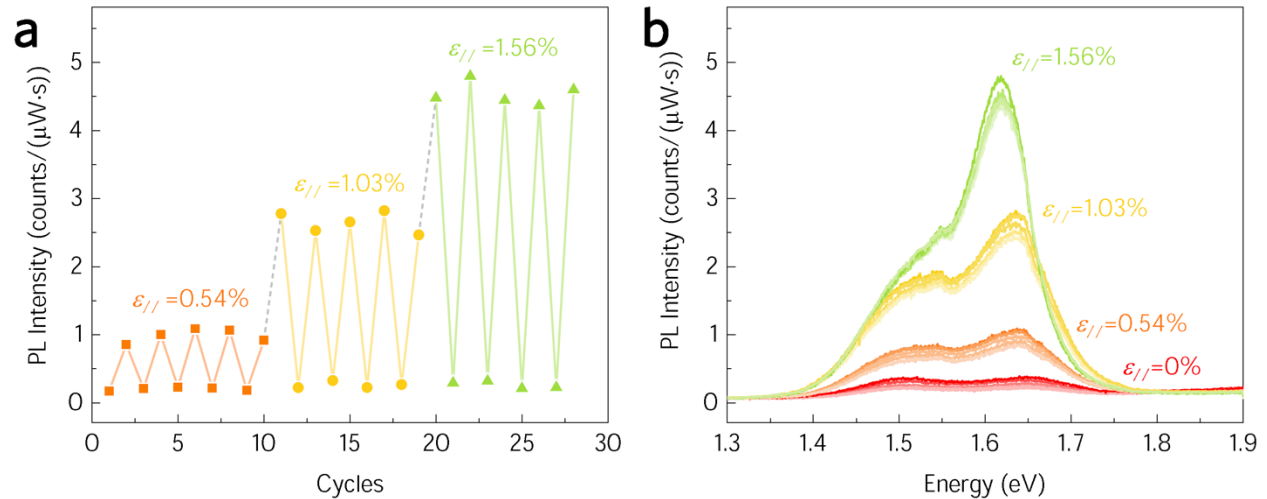
Figure S5. Reproducibility of strain-controlled photoluminescence (PL) emission spectra. *(a) Cyclic stability of the maximum PL intensities of bilayer WSe$_2$ at uniaxial strain, $\varepsilon_{//}$, demonstrating elastic and reversible strain up to 1.56%. (b) Corresponding PL spectra of cyclically strained bilayer WSe$_2$.*

It is critical to verify the amount of strain transferred from the flexible substrate to the WSe$_2$ sample. In this study, we have verified the strain transfer by measuring the Grüneisen parameter of monolayer graphene from the strain-dependent Raman spectra. The graphene was grown on

copper foil (Alfa Aesar #13382) by thermal catalytic decomposition of methane, similar to Ref. 10. The coating on the Cu foil is first removed with dilute nitric acid, where the pretreatment etching time is limited to prevent roughening of the Cu surface while removing the protective coating similar to what has been reported by Ref. 11. After pretreatment, the foil is loaded into a low pressure CVD reactor system and the growth is carried out at 1000°C for 20 minutes at ~333 mbar using 100 cm^3min^{-1} of H_2 and 1 cm^3min^{-1} of CH_4.

In contrast with a previous study[7], where only the bottom side of the exfoliated graphene was in contact with a SU-8/PET substrate, we encapsulated our graphene using PMMA (see section III, supporting information) to act as a control experiment to compare with WSe_2 bilayer. The Raman spectra was measured by a Horiba Multiline Raman Spectrometer-LabRAM HR Evolution. Since we were unable to resolve the G mode from the signal arising from the PMMA/PET substrate, we evaluated the Grüneisen parameter of dispersive in-plane transverse optical (iTO) phonons using the 2D mode of the sample and the three-dimensional Poisson effect model as described above (equation S11). Figure S6a,b show the evolution of the 2D peak with uniaxial strain. The linear strain dependence up to 1.56% strain indicates strain relaxation by slippage or plastic deformation is not observable. The difference in the slopes of the strain-dependent Raman shift between this work ($\delta\omega/\delta\varepsilon_{//}$ = -29.6±1.6 cm^{-1}/% strain) and Ref. 7 ($\delta\omega/\delta\varepsilon_{//}$ = -64.5±4.8 cm^{-1}/% strain) arises from the fact that our encapsulated graphene experiences an out-of-plane compressive stress due to the 3D Poisson effect of the substrate, while the graphene in Ref. 7 is unencapsulated. The uncertainty in $\delta\omega/\delta\varepsilon_{//}$ is given as the upper and lower 95% confidence bounds of the linear regression model used to fit the data. For our encapsulated graphene, we have obtained a value of γ_{2D} = 3.894 with a standard deviation of 0.214 (Figure S6c). The value we obtain is consistent with the value for the iTO modes we calculate by analyzing the 2D strain-dependent frequency shift reported in a

similar study on graphene[7], $\gamma_{2D} = 3.583 \pm 0.267$, where we have defined the uncertainty from the upper and lower 95% confidence bounds. In our analysis of Ref. 7, we do not consider the out-of-plane Poisson effect as the sample is not encapsulated, and the Grüneisen parameters are calculated as

$$\gamma_{2D,\text{non-encapsulated}} = -\frac{\Delta\omega_{0,2D}}{\varepsilon_{//}(1 - \nu_{\text{in-plane}})\omega_{0,2D}} . \tag{S12}$$

We have chosen a Poisson's ratio of 0.33 for the SU8-coated PET and Perspex substrates used in that study[7]. The small deviation of Grüneisen parameters likely arises from the uncertainty of the estimated Poisson's ratios of the different flexible substrates. For example, PET has a manufacturer-provided range of 0.37–0.44 for semi-crystalline PET, and PMMA has a range from 0.3–0.4. Additionally, we note the appropriateness of our 3D model as follows: if we were to adopt a two-dimensional Poisson effect model for our encapsulated samples as described by equation S12, the Grüneisen parameter of our graphene would be underestimated by roughly a factor of two.
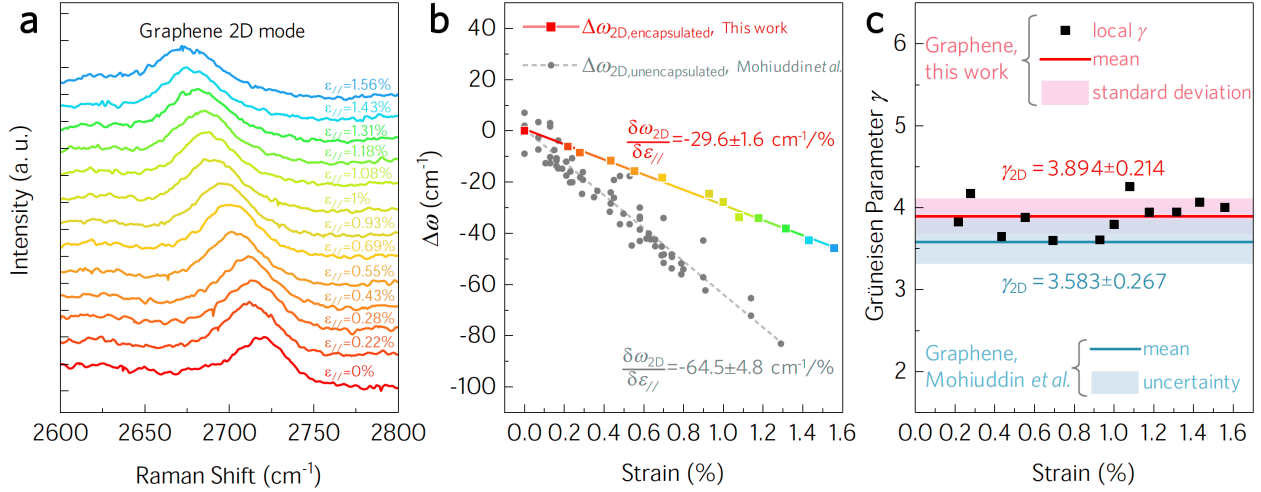
Figure S6. Measured Raman spectra and Grüneisen parameter of the 2D mode of CVD-grown encapsulated graphene. *(a) Raman spectra as a function of applied uniaxial strain. (b) Strain dependence of the 2D peak Raman shift, obtained by deconvolution of the experimental spectra using Lorentzian distributions. Also shown is the strain dependence of the 2D mode of unencapsulated graphene reproduced from Ref. 7. Uncertainties in $\delta\omega/\delta\varepsilon_{//}$ are given as the upper and lower 95% confidence bounds of a linear regression model for both data sets. The linear strain dependence of the Raman shift indicates no observable strain relaxation. (c) The Grüneisen parameter for the 2D mode is obtained from the strain-dependent Raman spectra as 3.894 with a standard deviation of 0.214. This is in agreement with the 2D mode value of 3.583±0.267 calculated from Ref. 7, where uncertainty is defined using the upper and lower 95% confidence bounds.*

VII. Photoluminescence (PL) spectra analysis

The PL emission spectra was deconvolved for each strain value using Gaussian distributions as shown in Figure S7. We note that the coefficient of determination (R^2) is high due to the low PL signal-to-noise ratio, 0.983 for the unstrained sample and higher than 0.997 for all strained cases.
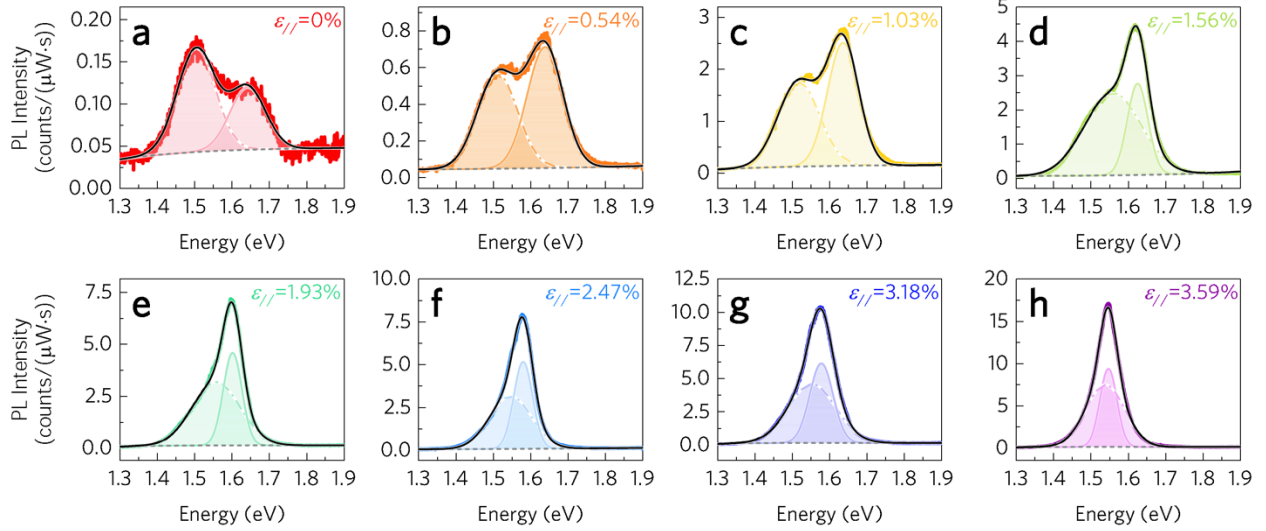
Figure S7. Photoluminescence spectra of bilayer WSe₂ with increasing uniaxial strain. *PL intensity versus emission energy is shown for $\varepsilon_{//}$ = (a) 0, (b) 0.54, (c) 1.03, (d) 1.56, (e) 1.93, (f) 2.47, (g) 3.18, and (h) 3.59% under continuous wave excitation at an energy of 2.33 eV (λ = 532 nm). The indirect (dash-dotted lines) and direct (solid lines) optical transition peaks were deconvolved using Gaussian distributions, and the background is shown as a gray dashed line.*

VIII. Density functional theory calculation of strain-dependent electronic band structure

DFT calculations were performed using projector augmented wave pseudo-potentials[12] as implemented in the VASP code[13]. The cutoff energy is 520 eV for the plane-wave expansions, and the Monkhorst–Pack *k*-point mesh is 15×15×1. The exchange-correlation functional is treated within the Perdew–Burke–Ernzerhof (PBE) generalized gradient approximations (GGA)[14]. The conventional DFT energy is supplemented with a pairwise interatomic vdW potential which is determined by Tkatchenko and Scheffler (TS-vdW) from non-empirical mean-field electronic structure calculations[15]. The TS-vdW parameterization has proven to be robust to describe the interlayer coupling for strain engineering in other 2D TMDs[16,17]. The atomic positions of a unit

cell (3 atoms) are optimized until all components of the forces on each atom are reduced to values below 0.01 eV/Å.

VIII. Theoretical prediction of the photoluminescence (PL) emission amplification

To estimate the PL intensity enhancement of the direct transition, we use a similar approach as reported in Ref. 18 and define the radiative efficiency η for the direct transition as[19]

$$\eta = \frac{Anp}{Anp + Bnp^2 + Cn}, \tag{S13}$$

where n is the electron concentration, p is the hole concentration, Anp represents radiative recombination, Bnp^2 represents Auger recombination, and Bn represents Shockley-Read-Hall recombination. The PL intensity of the direct electronic transition can be estimated as

$$I_{\text{direct}} \propto \eta \cdot \left(\frac{n_{\text{direct}}}{n_{\text{direct}} + n_{\text{indirect}}} \right) \cdot \left(n_{\text{direct}} + n_{\text{indirect}} \right), \tag{S14}$$

where n_{direct} and n_{indirect} are the electron concentrations at the direct and indirect conduction band minima, CBM$_{\text{direct}}$ and CBM$_{\text{indirect}}$, respectively. To estimate the PL intensity amplification, we simplify the above equation by assuming the radiative efficiency, η, remains constant with strain. The PL intensity enhancement can be expressed as

$$\frac{I_{\text{direct}}(\varepsilon_{//})}{I_{\text{direct}}(\varepsilon_{//} = 0)} = \frac{n_{\text{direct}}(\varepsilon_{//})}{n_{\text{direct}}(\varepsilon_{//} = 0)}. \tag{S15}$$

Using the Boltzmann approximation, we approximate n_{direct} using the strain-dependent direct electronic band gap obtained by our DFT-vdW calculations, ΔE_{direct}, as

$$\frac{I_{\text{direct}}(\varepsilon_{//})}{I_{\text{direct}}(\varepsilon_{//} = 0)} = \frac{e^{-\frac{\Delta E_{\text{direct}}(\varepsilon_{//})}{k_B T}}}{e^{-\frac{\Delta E_{\text{direct}}(\varepsilon_{//} = 0)}{k_B T}}}. \tag{S16}$$

A similar treatment can be used to predict attenuation of the indirect transitions as

$$\frac{I_{\text{indirect}}(\varepsilon_{//})}{I_{\text{indirect}}(\varepsilon_{//}=0)} = \frac{e^{-\frac{\Delta E_{\text{indirect}}(\varepsilon_{//})}{k_{\text{B}}T}}}{e^{-\frac{\Delta E_{\text{indirect}}(\varepsilon_{//}=0)}{k_{\text{B}}T}}} . \tag{S17}$$

IX. Supporting references

1. Wong-Ng, W., McMurdie, H. F., Paretzkin, B., Zhang, Y., Davis, K. L., Hubbard, C. R., Dragoo, A. L., & Stewart, J. M. Reference X-ray diffraction powder patterns of fifteen ceramic phases. *Powder Diffraction* **2**, 257–265 (1987). http://dx.doi.org/10.1017/S0885715600012926

2. Suk, J. W., Kitt, A., Magnuson, C. W., Hao, Y., Ahmed, S., An, J., Swan, A. K., Goldberg, B. B., & Ruoff, R. S. Transfer of CVD-grown monolayer graphene onto arbitrary substrates. *ACS Nano* **5**, 6916–6924 (2011). http://dx.doi.org/10.1021/nn201207c

3. Schneider, C. A., Rasband, W. S., & Eliceiri, K. W. NIH Image to ImageJ: 25 years of image analysis. *Nature Methods* **9**, 671–675 (2012). http://dx.doi.org/10.1038/nmeth.2089

4. Grüneisen, E. Theorie des festen Zustandes einatomiger Elemente. *Annalen der Physik* **344**, 257–306 (1912). http://dx.doi.org/10.1002/andp.19123441202

5. Dove, M. T. *Introduction to Lattice Dynamics* (Cambridge University Press, Cambridge, 1993). http://dx.doi.org/10.1017/cbo9780511619885

6. Kittel, C. *Introduction to Solid State Physics*, 8 ed. (Wiley, New Jersey, 2004). http://www.wiley.com/WileyCDA/WileyTitle/productCd-EHEP000803.html

7. Mohiuddin, T. M. G., Lombardo, A., Nair, R. R., Bonetti, A., Savini, G., Jalil, R., Bonini, N., Basko, D. M., Galiotis, C., Marzari, N., Novoselov, K. S., Geim, A. K., & Ferrari, A. C. Uniaxial strain in graphene by Raman spectroscopy: *G* peak splitting, Grüneisen parameters, and sample orientation. *Physical Review B* **79**, 205433-1–8 (2009). http://dx.doi.org/10.1103/PhysRevB.79.205433

8. Conley, H. J., Wang, B., Ziegler, J. I., Haglund, R. F., Jr., Pantelides, S. T., & Bolotin, K. I. Bandgap engineering of strained monolayer and bilayer MoS_2. *Nano Letters* **13**, 3626–3630 (2013). http://dx.doi.org/10.1021/nl4014748

9. Greaves, G. N., Greer, A. L., Lakes, R. S., & Rouxel, T. Poisson's ratio and modern materials. *Nature Materials* **10**, 823–837 (2011). http://dx.doi.org/10.1038/nmat3134

10. Chen, Y. L., Analytis, J. G., Chu, J.-H., Liu, Z. K., Mo, S.-K., Qi, X. L., Zhang, H. J., Lu, D. H., Dai, X., Fang, Z., Zhang, S. C., Fisher, I. R., Hussain, Z., & Shen, Z.-X. Experimental realization of a three-dimensional topological insulator, Bi_2Te_3. *Science* **325**, 178–181 (2009). http://dx.doi.org/10.1126/science.1173034

11. Kim, S. M., Hsu, A., Lee, Y.-H., Dresselhaus, M., Palacios, T., Kim, K. K., & Kong, J. The effect of copper pre-cleaning on graphene synthesis. *Nanotechnology* **24**, 365602-1–7 (2013). http://dx.doi.org/10.1088/0957-4484/24/36/365602

12. Blöchl, P. E. Projector augmented-wave method. *Physical Review B* **50**, 17953–17979 (1994). http://dx.doi.org/10.1103/PhysRevB.50.17953

13. Kresse, G. & Furthmüller, J. Efficient iterative schemes for *ab initio* total-energy calculations using a plane-wave basis set. *Physical Review B* **54**, 11169–11186 (1996). http://dx.doi.org/10.1103/PhysRevB.54.11169

14. Perdew, J. P., Burke, K., & Ernzerhof, M. Generalized gradient approximation made simple. *Physical Review Letters* **77**, 3865–3868 (1996). http://dx.doi.org/10.1103/PhysRevLett.77.3865

15. Tkatchenko, A. & Scheffler, M. Accurate molecular van der Waals interactions from ground-state electron density and free-atom reference data. *Physical Review Letters* **102**, 073005-1–4 (2009). http://dx.doi.org/10.1103/PhysRevLett.102.073005

16. Dong, L., Wang, J., Namburu, R., O'Regan, T. P., Dubey, M., & Dongare, A. M. Edge effects on band gap energy in bilayer 2H-MoS_2 under uniaxial strain. *Journal of Applied Physics* **117**, 244303-1–4 (2015). http://dx.doi.org/10.1063/1.4922811

17. McCreary, A., Ghosh, R., Amani, M., Wang, J., Duerloo, K.-A. N., Sharma, A., Jarvis, K., Reed, E. J., Dongare, A. M., & Banerjee, S. K. Effects of uniaxial and biaxial strain on few-layered terrace structures of MoS_2 grown by vapor transport. *ACS Nano* **10**, 3186–3197 (2016). http://dx.doi.org/10.1021/acsnano.5b04550

18. Desai, S. B., Seol, G., Kang, J. S., Fang, H., Battaglia, C., Kapadia, R., Ager, J. W., Guo, J., & Javey, A. Strain-induced indirect to direct bandgap transition in multilayer WSe$_2$. *Nano Letters* **14**, 4592–4597 (2014). http://dx.doi.org/10.1021/nl501638a

19. Sze, S. M. & Ng, K. K. *Physics of Semiconductor Devices*, 3 ed. (Wiley, New Jersey, 2006). http://dx.doi.org/10.1002/0470068329